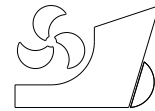


Bin Wang
Yuqi Jiao
Dongsheng Qiao
Shan Gao
Tianfei Li
Jinping Ou



<http://dx.doi.org/10.21278/brod74206>

ISSN 0007-215X
eISSN 1845-5859

Motion characteristics of vertically loaded anchor during drag embedment in layered clay

UDC 624.153.7:532.511
Original scientific paper

Summary

As a widely used taut-wire mooring system for deepwater platforms, the Vertically Loaded Anchor (VLA) has better performance in bearing capacity, angle adaptability, and deepwater installation than other systems. However, the installation process of the VLA and its motion characteristics are significantly impacted by multi-layered seabed soil. In this paper, the coupled Eulerian–Lagrangian (CEL) large deformation finite element analysis method has been applied to analyse the continuous penetration of a VLA in nonuniform clay with an interbedded stiff layer. A detailed parametric study has been carried out to explore the trajectory, drag angle, movement direction and drag force of the VLA in layered clay with different embedded depths, thicknesses and undrained shear strength of the stiff layer. The CEL numerical analysis results have been validated by comparison with the analytical solutions from the inverse catenary equation. Excellent agreement has been obtained between the results from the CEL analyses and the analytical solutions. The stiff layer leads to concave and convex shapes on the trend lines of the movement direction angle and drag forces, respectively. The embedded depth of the stiff layer determines where the concave and convex shapes appear on the trend lines, while the thickness affects the sizes of the openings of the shapes. The most decisive parameter, an abrupt variation in the undrained shear strength, causes predominant rotation at the interface of layered clay. It diminishes the final embedment depth and ultimate stable drag force, meaning that the bearing capacity of the VLA severely declined in layered clay.

Key words: *vertically loaded anchor; coupled Eulerian–Lagrangian method; layered clay; motion characteristic*

1. Introduction

With the exploitation of marine resources gradually advancing to deep waters, traditional anchor foundations cannot meet the requirements of deepwater mooring system designs, and vertically loaded anchors (VLAs) have been developed [1, 2]. Not only does the

VLA have superior performance in terms of low cost and simple construction, but it also has a flexible anchor shank that enables the anchor fluke to be in a normal loading state under ideal working conditions. Therefore, the pullout capacity can reach more than 100 times its weight to meet the design requirement [3]. Since the drag embedding process determines the ultimate embedding depth, movement direction of the VLA and ultimate bearing capacity of the upper platform, the drag embedding process must be accurately simulated [4, 5, 6, 7].

The installation process of a VLA by an anchor-handling vessel (AHV) is shown in Fig. 1. After the AHV is positioned, the mooring line and anchor are first slowly lowered into the water, with the stern tail lying flat on the seabed to regulate the orientation of the anchors and ensure that the initial drag angle is zero. Then, the mooring line is released to allow the VLA to drop to the seabed. When the mooring line is long enough, the tension rises, and the VLA is steadily drag-embedded in the seabed by the towing action of the AHV. The shank of the VLA is no longer operative when the drag force of the mooring line reaches the installation load, which allows the VLA to transition from the installed state to the normal stressed working state.

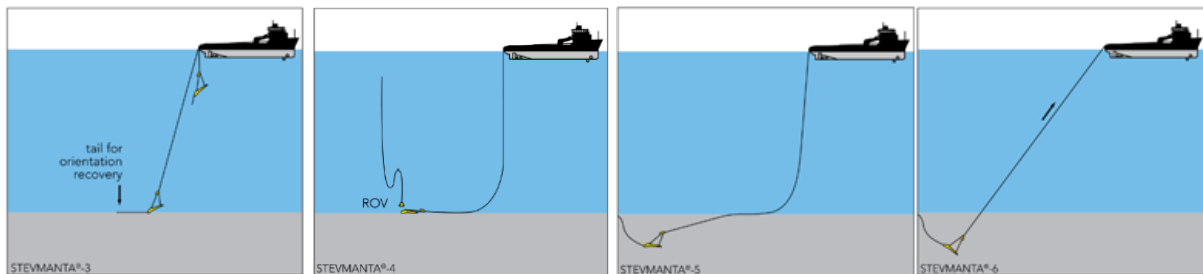


Fig. 1. The installation process of the VLA employing an anchor-handling vessel

Currently, the principal methods for predicting the drag trajectory of anchors are the model test method, analytical method and numerical simulation. Vryhof and Bruce have carried out numerous on-site tests and laboratory model tests [8]. However, on-site tests are neither universally applicable to all geological conditions nor do they completely reveal the soil flow mechanisms during drag installation. Additionally, these model tests conducted on 1g conditions [9, 10, 11, 12, 13, 14, 15, 16] cannot maintain stress similar to that on-site circumstances. Although the geotechnical centrifuge test [17] can compensate for the shortcomings of model tests, it is costly. Two more commonly used analytical methods, the limit equilibrium method [18, 19, 20, 21, 22] and the plastic upper bound method [23, 24, 25], are efficient to derive and apply, but usually include assumptions of small deformation and no self-weight of mooring systems that make the analytical results significantly different from reality. The installation process of a VLA always involves large deformations of the soil, which requires the large deformation finite element (LDFE) method to address mesh distortion and contact problems. Remeshing and interpolation techniques with the small strain (RITSS) method [26, 27, 28] and the coupled Eulerian–Lagrangian (CEL) method [29, 30, 31] are two effective ways to analyse large deformation problems in marine geotechnics. However, the RITSS method is based on many internal codes, which makes it hard to extend to the simulation of the VLA. More recently, the CEL method was used to simulate the drag embedment procedure of a mooring foundation and its interaction with the seabed soil, and the results validated and demonstrated the reliability of these numerical simulation methods to investigate the motion characteristics of VLAs [32, 33].

According to geological surveys, layered soils are widely distributed in offshore areas around the world, such as Southeast Asia, India, the Arabian Gulf, and the Gulf of Mexico [34, 35]. The presence of a stiff layer in soft clay complicates the installation process of offshore foundations and is detrimental to the stability of a foundation in service status [36].

To explore the tension transmitting and profile properties of anchor lines embedded in layered soils, Liu et al. [37] proposed a mechanical model and analytical procedures based on the inverse catenary equation. Peng et al. [29, 38] developed an analytical method to model the behaviour of drag anchors in sand, clay and multi-layered soils. Adopting a model test, Lai et al. [39] revealed the drag embedment behaviours of drag anchors in layered clay with a stiff layer interbedded in soft clay, and the results showed that the stiff layer significantly increased the difficulty of drag embedment.

In general, the mentioned studies on the drag trajectories of mooring foundations in homogeneous and layered soils were mainly focused on model tests and analytical methods, whereas LDFE analysis methods were quite limited, especially for the trajectory of VLA in nonuniform clay with an interbedded stiff layer. This present work adopts the CEL method in ABAQUS/Explicit [40] to develop an anchor-chain-soil interaction model. The motion characteristics of the VLA during drag embedment in nonuniform clay with an interbedded stiff layer are investigated, which considers the effects of the stiff layer depth, thickness and strength on the trajectory, drag angle, movement direction and drag force. The numerical model will hopefully facilitate the analysis of the drag trajectory of VLAs and provide scientific foundations for the installation of VLAs in practice.

2. Numerical analysis

2.1 Anchor chain and VLA model

To simulate the axial tension of the anchor chain of a taut-wire mooring system, the anchor chain was discretized into a series of rigid cylinders, as shown in Fig. 2. Abaqus/Link connections ensured that the anchor chain model transmitted only axial force and no bending moments and maintained a constant length. In addition, to achieve a sufficient discrete degree of the anchor chain, an 18 m long anchor chain was discretized into 30 segments of rigid cylinders with a diameter $d_s=0.1$ m, a length $l_s=5.0d_s$ and a length of link connections $s_s=1.0d_s$. The specific parameters are shown in Fig. 2.

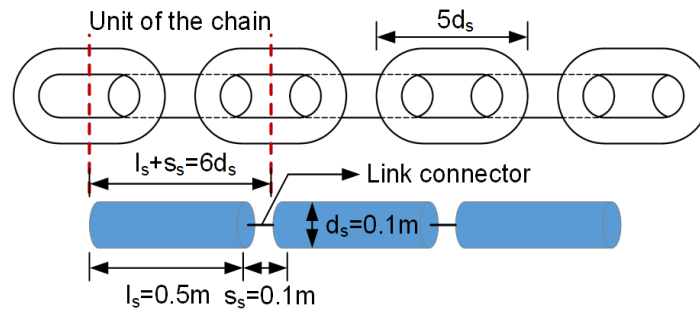


Fig. 2. Anchor chain numerical model

A simplified VLA model was established with the design parameters provided by Vrhof to achieve efficient computing. The fluke was replaced by a rectangular plate with an equivalent length of $l_a=2.236$ m, a width of $B_a=1.118$ m and a thickness of $t_a=0.17$ m, as shown in Fig. 3. The shackle was simplified to a mass point due to its relatively small size. The shanks were converted into a series of link connections to transmit the axial force with the projection length in the horizontal direction of $E_0=3$ m. In addition, to simulate the initial state of the drag embedment, the procedure of sinking the VLA to the seabed was omitted, and the fluke was directly positioned on the seabed surface at an initial angle of $\theta_s=45^\circ$.

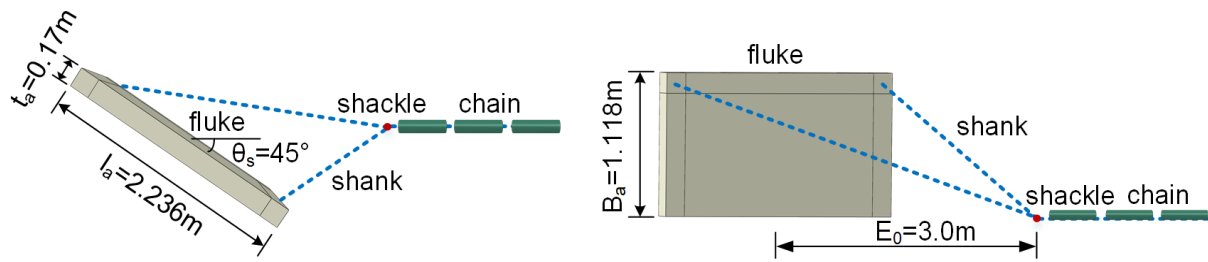


Fig. 3. VLA numerical model

2.2 Seabed soil model

Since the coupled Eulerian–Lagrangian (CEL) analysis in ABAQUS/Explicit was for 3D elements only, half of the soil domain was involved in the analysis accounting for the inherent symmetry, as shown in Fig. 4. To accommodate the chain length, the soil domain was divided into two areas with widths of $W_{s1}=3.0\text{ m}$ and $W_{s2}=0.85\text{ m}$, lengths of $L_{s1}=47.0\text{ m}$ and $L_{s2}=38.0\text{ m}$ and depth of $H_s=13.0\text{ m}$, which was shown to be sufficiently large to avoid boundary effects. A 2.0 meter-thick layer of void elements was defined above the soil surface to accommodate potential soil heave during the drag embedment of the VLA. The soil was modelled as a linear elastic-perfectly plastic material obeying a Tresca yield criterion with an effective unit weight $\gamma'=6.8\text{ kN/m}^3$ and a uniform stiffness ratio $E/s_u=500$. Considering the relatively fast embedment of VLAs in the field, all the analyses simulated undrained conditions and adopted Poisson's ratio $\nu=0.49$.

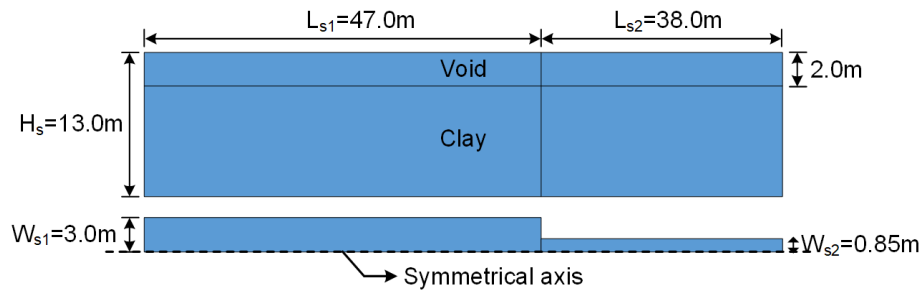


Fig. 4. Seabed soil model dimensions

2.3 Anchor chain-seabed soil model

The anchor-chain-soil interaction model was performed using the CEL approach in ABAQUS/Explicit. Fig. 5 depicts the initial arrangement of the model, in which the fluke was positioned on the seabed surface at an initial angle of 45° and the anchor chain was straightened horizontally. A constant loading velocity was applied at the end of the anchor chain to ensure computational efficiency while reducing oscillations in the results, and the fluke rotated and penetrated under the combined action of gravity and drag force until the drag was completed.

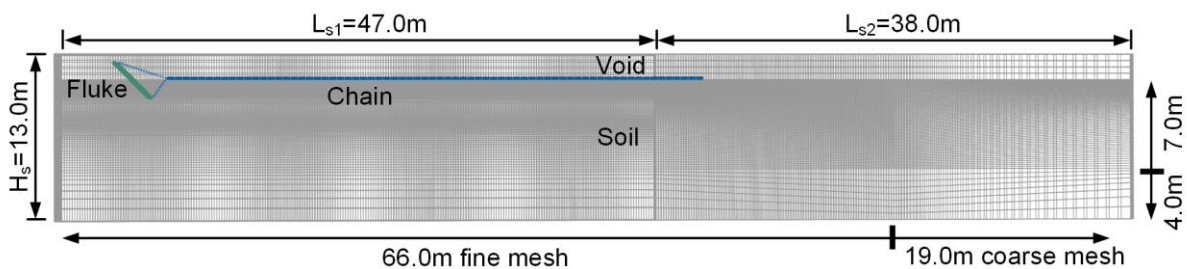


Fig. 5. The anchor-chain-soil model and typical mesh used in CEL analysis

Since the magnitude of this loading velocity impacts the installation process of VLA, the drag trajectories are measured for three scenarios of velocity 1.0 m/s, 0.5 m/s, and 0.25 m/s, respectively. Fig. 6 presents the trajectories of various velocity differ conspicuously at the early drag stage, but the final penetration depth converges with the increase of horizontal drag distance. When the drag velocity is below 0.5, reducing it further has less than a 3% impact on outcomes, thus verifying the convergence of the drag velocity.

Additionally, the fluke and the chain were modeled as rigid Lagrangian bodies, while the soil domains were set to Eulerian elements. Interactions between the Eulerian soil domain and the rigid Lagrangian bodies were considered by a penalty contact algorithm with hard contact in normal and a tangential friction coefficient of $\mu=0.1$. The continuous elements of C3D8R and the Eulerian brick elements of EC3D8R were used to discretize the rigid bodies and the soil domains, respectively, in which the graded mesh was used with fine mesh in the vicinity of the VLA movement area of the soil domain and coarse mesh in the outer position, and the mesh sizes of the fluke and anchor chain were set according to their geometric features, as shown in Fig. 5. To establish boundary conditions, soil flows normal to the vertical faces and the base of the soil domain was set to zero, and no flow of material was permissible in and out of the exterior vertical surface.

The sensitivity analysis of mesh size has been conducted along the three mesh division schemes depicted in Table 1 by encrypting the mesh area below the fluke. The trajectory performances given in Fig. 7 illustrate that when the total number of soil meshes was 630,000 with a global size of $l_s/4$, increasing the number of mesh further has less than a 1% effect on penetration depth, indicating mesh convergence. A massive number of meshes also led to a long computation time for the numerical model. The computational time for a working condition was approximately 97200 s (equal to 27 hours) on a computer with an AMD processor of 64 cores and 256 G of random access memory.

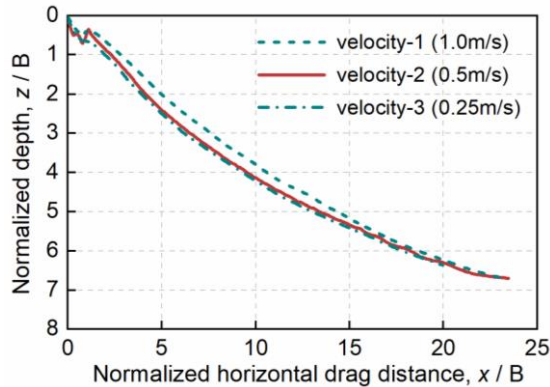


Fig.6 The trajectories of various velocity of VLA

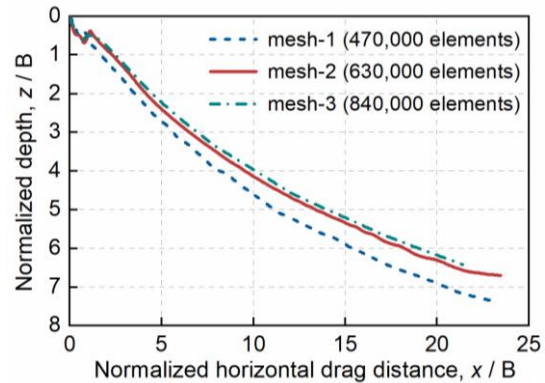


Fig.7 Mesh convergence of the numerical model

Table 1 Meshing for the numerical model

(a) Soil mesh division

case	Mesh density in the vertical direction of VLA movement			Global mesh	Mesh number
	Below chain and shank	Below fluke	Outside fluke		
Mesh-1	$d_s/4$	$d_s/4 \sim l_a/15$	$B_a/10$	$l_s/4$	840,000
Mesh-2	$d_s/4$	$d_s/4 \sim l_a/10$	$B_a/10$	$l_s/4$	630,000
Mesh-3	$d_s/4$	$d_s/4 \sim l_a/8$	$B_a/10$	$l_s/4$	470,000

(b) Fluke mesh division

Length direction	Width direction	Thickness direction	Mesh number
$l_a/20$	$B_a/10$	$t_a/2$	190

(c) Anchor chain mesh division

Length direction	Width direction	Mesh number
$l_s/5$	$d_s/2$	360

2.4 Validation of the numerical model

In previous studies, many scholars used the inverse catenary state equation to solve for the drag force of the anchor chain [18, 21, 41, 42]. A schematic diagram of the forces acting on the embedded chain element is shown in Fig. 8. The differential equations governing the embedded section of the chain are:

$$\frac{dT}{ds} = F + w \sin \theta \quad (1)$$

$$T \frac{d\theta}{ds} = -Q + w \cos \theta \quad (2)$$

where T is the tension in the chain; θ is the angle subtended by the chain to the horizontal; s is the distance measured along the chain; w is the buoyant weight of the chain per unit length; Q is the soil resistance normal to the chain; and F is the soil resistance tangential to the chain.

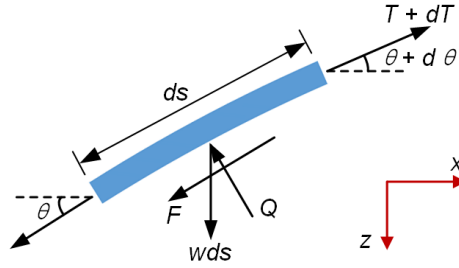


Fig. 8 Forces acting on the embedded chain element

The soil resistance can be further expressed in terms of the average normal pressure, q , and friction, f , multiplied by an effective width, as follows:

$$Q = (E_n d_s) \cdot q = E_n d_s N_c s_u \quad (3)$$

$$F = (E_t d_s) \cdot f = E_t d_s s_u \quad (4)$$

where E_n and E_t are multipliers to give the effective widths in the normal and tangential directions, respectively; N_c is the bearing capacity factor of the mooring line; and s_u is the undrained shear strength of the clay.

The friction force per unit length can be expressed as:

$$F = \mu Q \quad (5)$$

where μ is the frictional coefficient that lies in the range from 0.1 to 0.6 [16, 19].

Eq. (1) and Eq. (2) are combined, substituting Eq. (5), to give:

$$\frac{dT}{ds} + \mu T \frac{d\theta}{ds} = w(\sin \theta + \mu \cos \theta) \quad (6)$$

Ignoring the chain weight, Eq. (6) can be integrated to give the drag force profile as:

$$T = T_a e^{\mu(\theta_a - \theta)} \quad (7)$$

where T_a is the chain tension at the attachment point and θ_a is the attachment angle.

Substituting Eq. (7) into Eq. (2) and integrating this equation can lead to:

$$\frac{T_a}{1 + \mu^2} \left[e^{\mu(\theta_a - \theta)} (\cos \theta + \mu \sin \theta) \right]_{\theta}^{\theta_a} = \int_z^{z_a} N_c E_n d_s s_u dz \quad (8)$$

where z_a is the depth of the attachment point; z is the drag anchor embedded depth; and z_a and θ_a are calculated by the finite element analysis.

In Eq. (8), the bearing capacity factor N_c can be calculated by Eq. (9-10) [43]:

$$N_{cs} = 2 + (N_{cd} - 2) \left(\frac{w}{w_{deep}} \right)^p \quad (9)$$

$$p = 0.61 \left(\frac{s_u}{\gamma' d_s} \right)^{-0.31} \quad (10)$$

where N_{cs} is the shallow bearing factor; N_{cd} is the deep bearing factor, taken as 9.8 in this paper; w is the embedment depth; and w_{deep} is the transition depth, adopted to be 3.5 m in this study.

The drag trajectory and drag force comparison between the CEL numerical simulation and the analytical solutions derived from the inverse catenary equation in uniform clay with constant undrained shear strength $s_u=7.0$ kPa are shown in Fig. 9. With the parameters of the bearing capacity factors N_{cl} and N_{cf} for the anchor chain and fluke varying in the ranges (7.6, 14) and (7.6, 11.8), respectively, the upper and lower bounds of the trajectory predicted by Liu et al. [40] are presented in Fig. 9 (a). This demonstrates that the drag trajectory calculated by the present study was between the upper and lower bounds of the analytical solution of Liu et al. [44], which illustrates the feasibility of the numerical model to predict the drag trajectory. Fig. 9 (b) reveals that the drag force obtained by the inverse catenary equation first decreases and then increases in the early stage of the drag embedment process, which differed from the realistic where the drag force started from zero and gradually increases to the ultimate value. The numerical results were deemed to be more appropriate. It is the assumptions of the inverse catenary equation that ignore the weight of the anchor and set the catenary angle at the seabed surface to be zero that led to discrepancies between the numerical and analytical results in the horizontal drag distance of less than 10 m. However, as the VLA embedded more deeply, the numerical result successfully captured the drag force observed in the inverse catenary equation, which thus verified the accuracy of the numerical analysis.

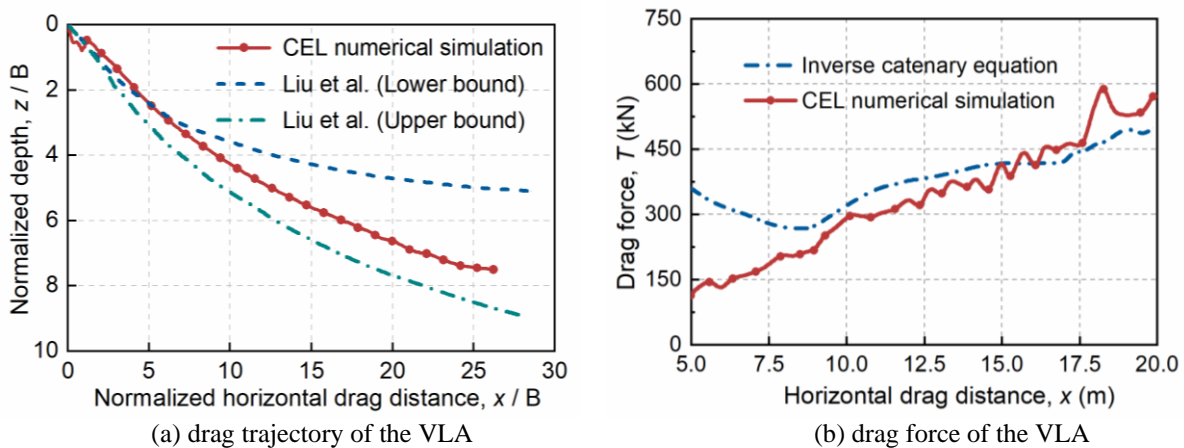


Fig. 9. Validation and comparison of results from the CEL numerical simulation and analytical solutions

3. Numerical analysis

3.1 Summary of numerical analyses

The motion characteristics of the VLA are significantly affected by the multi-layered seabed soil. A typical undrained shear strength distribution of nonuniform clay with an interbedded stiff layer is shown in Fig. 10, where the intermediate layer of clay with nonuniform undrained shear strength $s_{u2}=s_{ut2}+kz$ is interbedded in the clay of nonuniform undrained shear strength $s_u=s_{um}+kz$ with undrained shear strength at the second-third layer interface $s_{ut3}=s_{um}+kz$, and infinite depth; d is the embedded depth of the stiff layer of clay; t is the thickness of the stiff layer, s_{um} is the undrained shear strength at the first layer surface; s_{ub1} is the undrained shear strength at the base of the first layered clay, ditto for s_{ub2} ; s_{ut2} is the undrained shear strength of the stiff layer at the first-second layer interface, ditto for s_{ut3} .

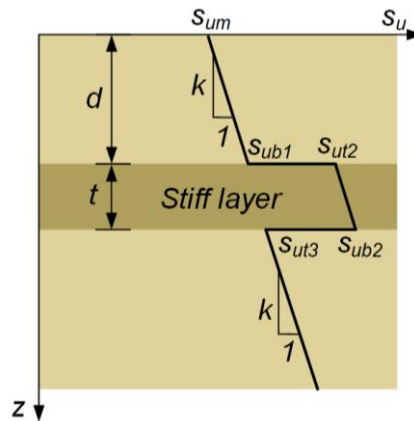


Fig. 10 The undrained shear strength of nonuniform clay with an interbedded stiff layer

The selected parameters for this study are assembled in Table 2 considering the offshore geotechnical properties and dimensions of the anchors. Uniform clay with constant undrained shear strength $s_u=5$ kPa was adopted as a control group (Group I, Table 2). For nonuniform clay with an interbedded stiff layer, the undrained shear strength at the seabed surface was selected as $s_{um}=5$ kPa with the strength gradient $k=1.4$ kPa/m, so that the inhomogeneity factor was taken as $kd_s/s_{um}=0.028$. The embedded depths and thicknesses of the stiff layer relative to the anchor chain diameter were taken as $d/d_s=10, 22.36, 30$ and $t/d_s=10, 22.36, 30$ (Groups II and III, Table 2), and the differences in undrained shear strength at the first-second layer interface were taken as $s_{ut2}-s_{ub1}=10$ to 20 kPa (Group IV, Table 2) to investigate their effect on the motion behaviours of the VLA.

Table 2 Classification of layered soil working conditions

Analysis	kd_s/s_{um}	t/d_s	d/d_s	$s_{ut2}-s_{ub1}$ (kPa)	Remarks
Group I	0	—	—	—	Uniform clay as a control group
Group II	0.028	10, 22.36 and 30	10	10	Exploration of the effect of the thickness of the stiff layer
Group III	0.028	10	10, 22.36 and 30	10	Exploration of the effect of the embedment depth of the stiff layer
Group IV	0.028	10	10	10 and 20	Exploration of the effect of the undrained shear strength at the first-second layer interface

3.2 Drag embedment process of the VLA in nonuniform clay with an interbedded stiff layer

The drag embedment behaviours of the VLA can be described as penetration along the movement direction of the fluke θ_m and rotation around a rotational centre R_c ; for the latter, it does not always coincide with the barycentre of the fluke (B_c). During the initial embedment stage, the VLA flips violently to adjust its angle and then penetrates into the upper layer. Fig. 11 depicts the distribution of the forces acting on the fluke during the stable embedding phase, which can be divided into two categories. One category is the forces vertical to the fluke, including the drag force T ; the component of the fluke weight $\cos\theta_s \cdot W_f$; soil pressure acting on the fluke F_p ; and the bonding force behind the fluke caused by the clay cohesion F_c and friction resistance of the fluke sidewall F_{fs} . The other is the forces parallel to the fluke, including the end bearing resistance of the fluke F_b , the shear force of the fluke surface F_s and the component of the fluke weight $\sin\theta_s W_f$.

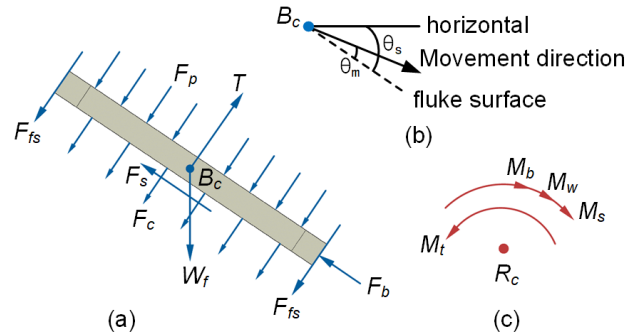


Fig. 11. Mechanical model of a VLA ((a) distribution of the forces, (b) angle schematic, (c) bending moment

Fig. 12 shows the Mises stress nephograms of the VLA embedded in nonuniform clay with an interbedded stiff layer, which was exported from the post-processing of ABAQUS visualization. When the fluke reached the interface of the soft-stiff layer (Fig. 12 (a)), the undrained shear strength s_u exhibited an abrupt increment so that the friction resistance F_{fs} and shear force F_s present on the upper part of the fluke were greater than those on the lower part. The total clockwise bending moments acting on the rotational centre R_c were greater than the counterclockwise bending moments. The combination of the two effects caused a predominantly clockwise rotation at the soil interface of the soft-stiff layer. During the period when the VLA was embedded in the stiff layer (Fig. 12 (b)), its movement was dominated by penetration, while the penetrating velocity gradually decreased due to the higher soil resistance. When the fluke penetrated through the stiff layer and entered the soft layer (Fig. 12 (c)), the angle of the fluke to the horizontal θ_s further decreased owing to counterclockwise rotation at the interface of the stiff-soft layer. The installation process was completed when the drag angle θ_a approached the design angle of the shackle and the drag force simultaneously reached the installation load.

In general, the motion of the VLA in the homogeneous soil layer was dominated by penetration and rotation at the soil interface. The rotation direction of the fluke was determined by the relative magnitude of the undrained shear strength above and below the soil interface. The deposit of the stiff layer affected the movement direction of the fluke, which resulted in several angle adjustments to reach the VLA design angle during installation, which would complicate the installation process of the VLA.

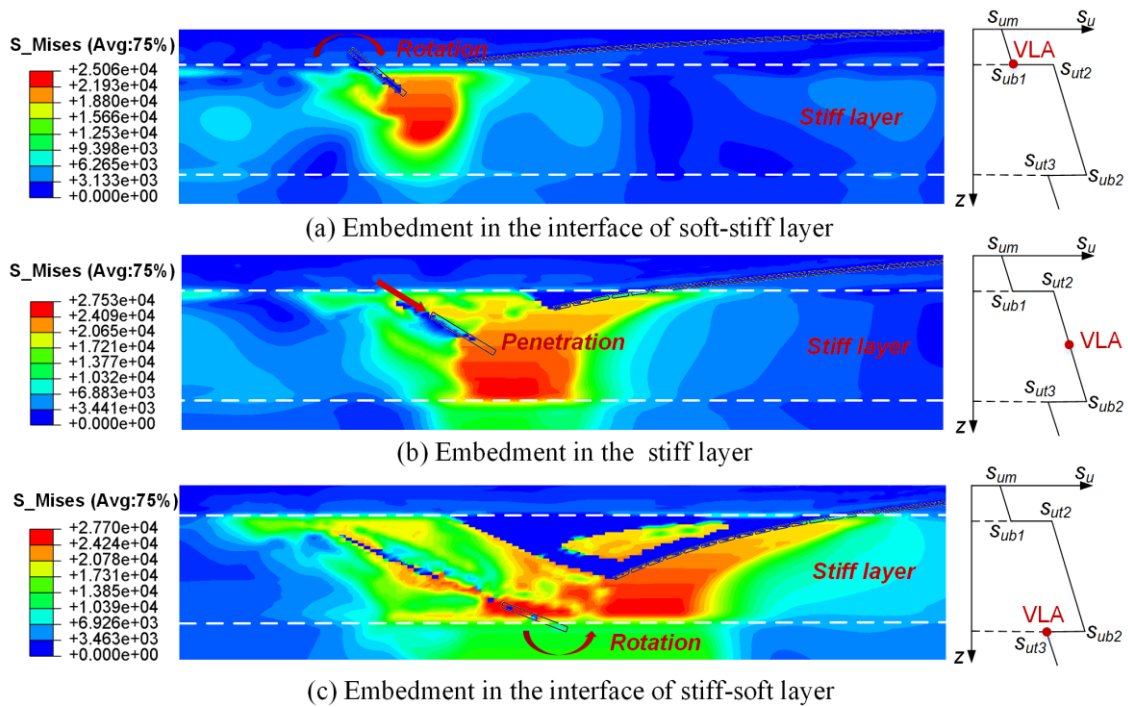


Fig. 12 The Mises stress nephograms of the VLA embedded in layered clay

4. Parametric study

4.1 Drag trajectory

The drag trajectory of the VLA could be displayed by schematic diagrams with horizontal drag distance on the horizontal axis and embedded depth on the vertical axis. Fig. 13 (a) suggests that the velocity of the VLA would decrease when it penetrated into the stiff layer. This was because the drag trajectories almost coincided at shallow penetration depths, but as the VLA penetrated into the stiff layer, the penetration depth became significantly shallower with the same horizontal drag distance. It also shows that the final embedded depths of VLA in the layered clay were relatively shallow compared to the circumstances in uniform clay. The causes were manifold. The depth of the stiff layer affected the movement direction of the fluke when it penetrated into the stiff layer. However, the thickness and the undrained shear strength of the stiff layer determined the rotational behaviour and penetration velocity of the anchor below the soft-stiff interface. The combination of the above resulted in a 4% to 22% reduction in final embedment depth when the VLA penetrated into the layered clay. The impacts of the depth, thickness and strength of the stiff layer on the motion characteristics of the VLA have been discussed, and the undrained shear strength of the stiff layer was the crucial factor.

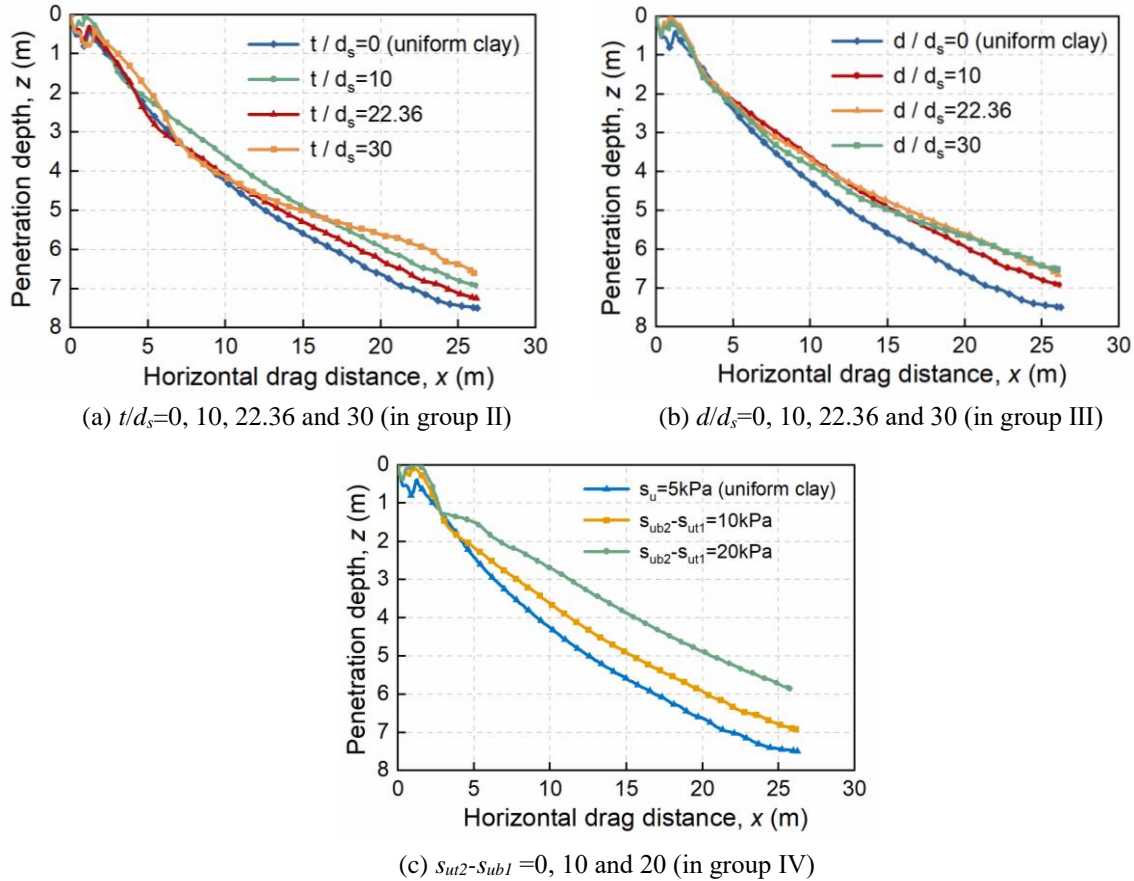


Fig. 13. Effect of the stiff layer on the drag trajectory of the VLA

4.2 Drag angle

To quantify the rotational behaviours of the anchor, the drag angles at the shackle relative to the top surface of the fluke were introduced, as presented in Fig. 14 (a). The fluke no longer rotated when the drag angle θ_a was approximately equal to the designed shackle angle (in this case, the designed shackle angle was 45°).

During the initial drag embedment phases, the fluke flipped rapidly, resulting in a large variation in drag angle as it first decreased and then increased. With further embedment, the fluke was completely embedded in the soil, and the rotational behaviour gradually increased. However, the stiff layer caused a significant difference. Due to the rotational behaviour of the VLA demonstrated in Fig. 12, the drag angle peaked at the interface of the soft-stiff layer and was slightly more than 45° . With further drag embedment, the drag angle stabilized in a fluctuating pattern. Moreover, the peak drag angle mainly depended on the strength of the stiff clay, the embedded depth of the stiff layer primarily affected the drag distance corresponding to the peak drag angle, and the presence of the stiff layer diminished the ultimate stable drag angle.

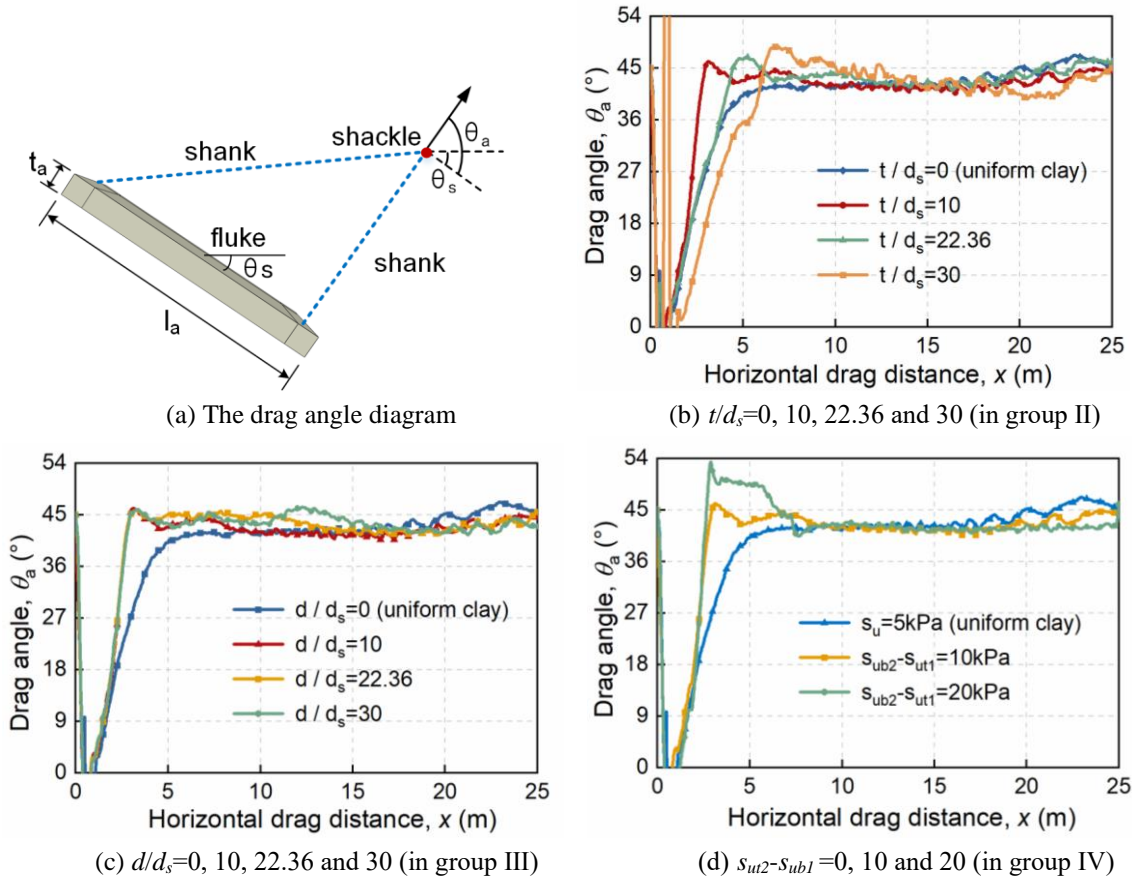


Fig. 14. Effect of the stiff layer on the drag angle of the VLA

4.3 Movement direction angle

The penetration behaviours of the VLA were usually along the movement direction angle θ_m , which denoted the movement angle of the fluke relative to the top surface of the fluke, as shown in Fig. 15(a). The relationships between the movement direction angle θ_m and the horizontal drag distance depicted in Fig. 13 demonstrate that the stiff layer of clay led to a significant concave trend of θ_m . The embedded depth of the stiff layer determined where the concave shape appeared on the tendency line of θ_m . The thickness of the stiff layer slightly affected the size of the concave opening. The undrained shear strength of the stiff layer was the decisive factor in the lower limit of the concave and its opening. The results shown in Fig. 15(d) supported this conclusion further by doubling the differential strength of the soft-stiff layer interface, and the movement direction angle θ_m decreased by more than 2 times because the higher soil strength required a longer drag distance for adjusting the movement direction as the anchor penetrated through the stiff layer. As the VLA moved along the top surface of the fluke, the movement direction angle θ_m eventually converged to zero. It is worth noting that the change in the movement direction angle was more sensitive to the presence of the stiff layer compared with the drag angle.

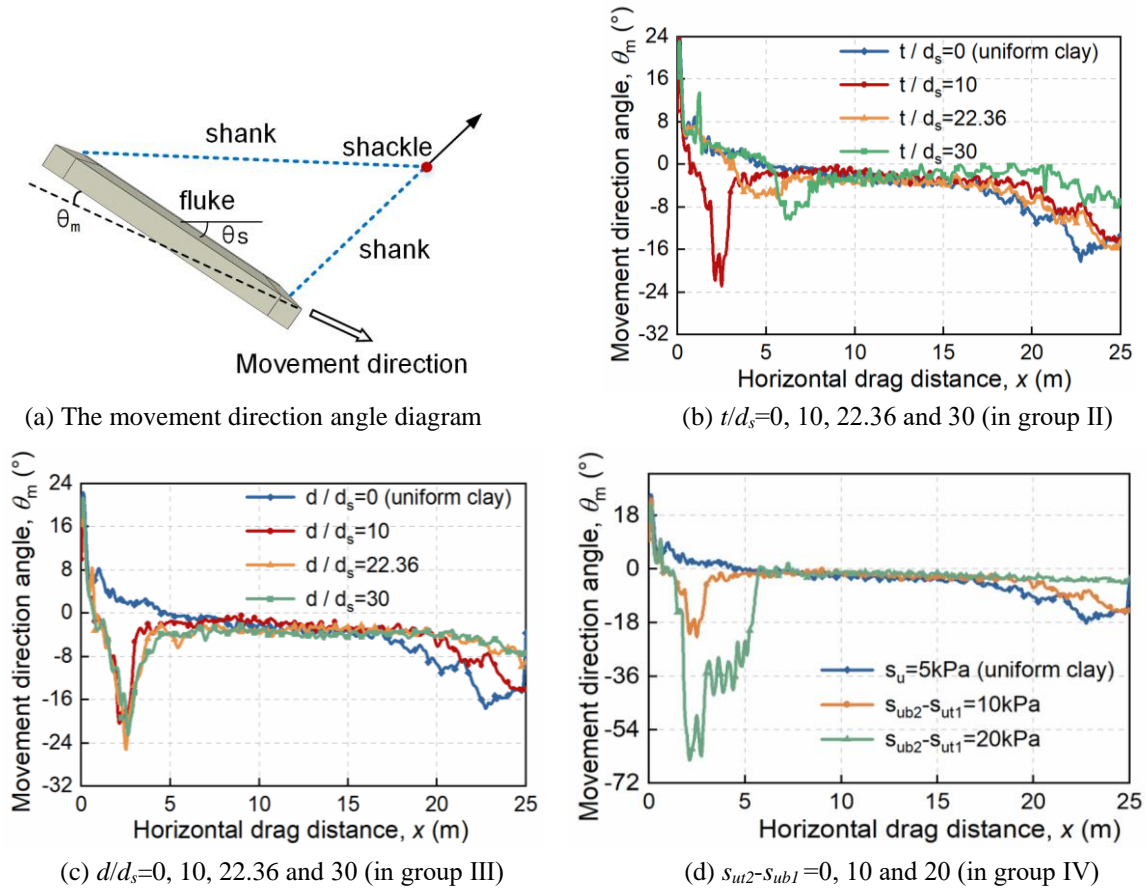


Fig. 15. Effect of the stiff layer on the movement direction of the VLA

4.4 Drag forces

The drag forces exerted at the shackle of the VLA increased by 1 to 3 times and presented a convex shape on the tendency line when the shackle penetrated into the stiff layer of clay, as shown in Fig. 16. However, after the anchor penetrated through this layer, the drag force decreased to less than that of the uniform clay. It seems that the embedded depth of the stiff layer had the most significant effect on the drag force, as inferred from Fig. 16. For a working condition with the normalized embedded depth of the stiff layer $d/d_s=30$, $t/d_s=10$ and $s_{ut2}-s_{ub1}=10$ kPa (Fig. 16 (a)), the drag force was steady after the horizontal drag distance reached 10 m, and the ultimate drag force was only 48% of that of the uniform clay, which meant that the bearing capacity of the VLA significantly declined as the embedded depth of the stiff layer increased. When the embedded depth was taken to be the same, the size of the convex opening on the tendency line of the drag force depended on the thickness of the stiff layer, as depicted in Fig. 16 (b), and the ultimate drag force was determined by the undrained shear strength. Fig. 16 (c) also suggests that doubling $s_{ut2}-s_{ub1}$ could lead to a 30% decrease in the ultimate drag force.

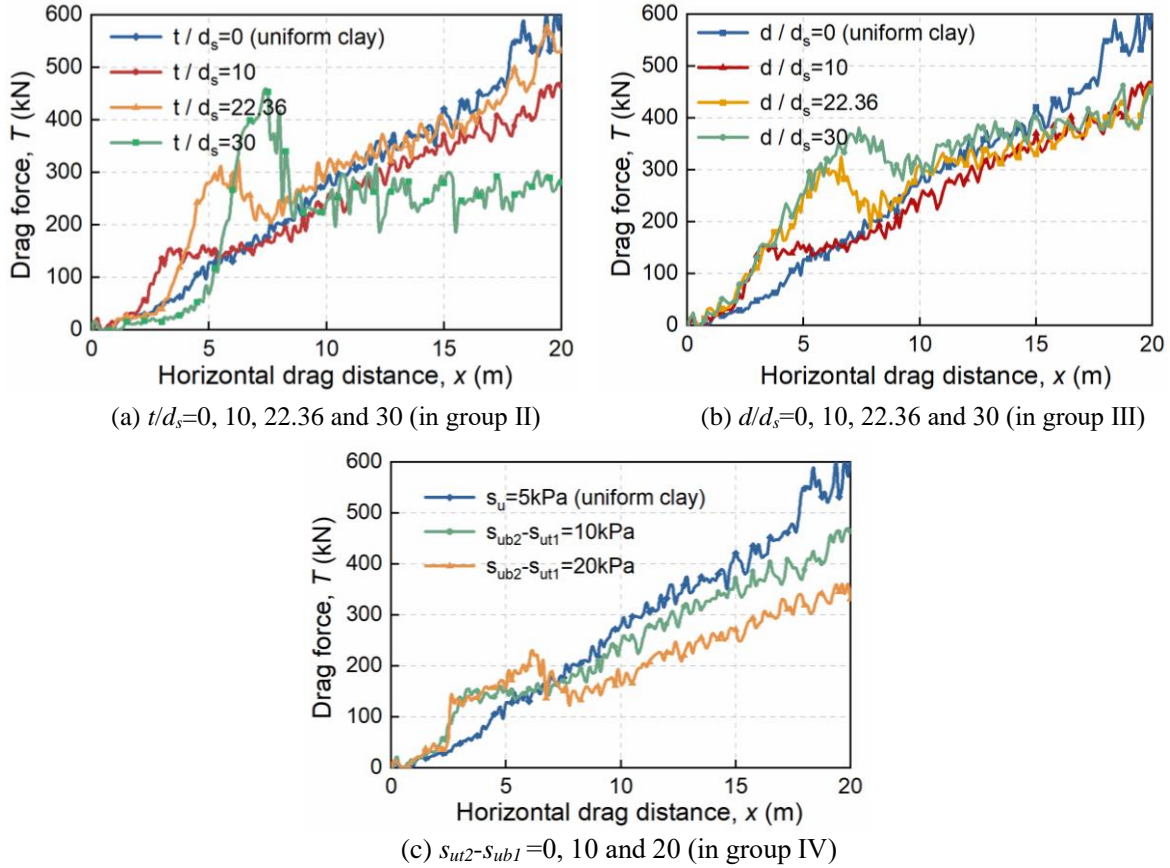


Fig. 16. Effect of the stiff layer on the drag force of the VLA

5. Conclusions

This paper reported the results of analyses using LDFE to investigate the motion characteristics of a VLA during drag embedment through nonuniform clay with an interbedded stiff layer. The CEL large deformation finite element analysis method was applied to model behaviour as the VLA penetrated continuously from the seabed surface. The numerical analysis results of the drag force profiles were validated against corresponding results obtained with the inverse catenary equation. The mechanisms of drag embedment in layered clay were revealed. The effects of the embedded depth, thickness and undrained shear strength of the stiff layer on the trajectory, drag angle, movement direction and drag force of the VLA were explored.

Overall, the CEL numerical analysis successfully captured the results from the inverse catenary equation. The abrupt variations in the undrained shear strength caused predominant rotations at the interfaces of clay layers. The stiff layer significantly affected the motion characteristics of the VLA, and the conclusions were as follows.

(1) The undrained shear strength of the stiff layer was the crucial factor that affected the drag trajectory of the VLA. The parameters studied in this paper resulted in from 4% to 22% reduction in final embedment depth compared to the circumstances in uniform clay. The drag trajectory of the VLA implied a reduction in the penetration velocity in a stiff layer of the layered clay.

(2) The drag angle θ_a peaked at the interface of the soft-stiff layers. The peak drag angle mainly depended on the strength of the stiff clay, the embedded depth of the stiff layer primarily affected the horizontal drag distance corresponding to the peak drag angle, and the presence of the stiff layer diminished the ultimate stable drag angle.

(3) The stiff layer of the layered clay led to a significant concave trend of the movement direction angle θ_m . The embedded depth of the stiff layer determined where the concave shape appeared on the tendency line of θ_m . The undrained shear strength of the stiff layer was the decisive factor in the lower limit of the concave trend and its opening. Doubling the differential strength of the soft-stiff layer interface caused a more than 2-fold reduction in the movement direction angle θ_m .

(4) Among the parameters studied in this paper, the drag forces exerted at the shackle increased by 1 to 3 times and presented a convex shape on the tendency line when the VLA penetrated into the stiff layer of clay. The size of the convex opening on the tendency line depended on the thickness of the stiff layer. Doubling the differential strength of the soft-stiff layer interface led to a 30% decrease in the ultimate drag force.

ACKNOWLEDGEMENTS

This work was supported by the National Natural Science Foundation of China [Grant Nos 51890915, 52071301 and 52101333] and the Fundamental Research Funds for the Central Universities.

REFERENCES

- [1] Tang, Y. G., Hu, J., Liu, L. Q., 2011. Study on the dynamic response for floating foundation of offshore wind turbine. *Proceedings of the ASME 2011 30th International Conference on Ocean, Offshore and Arctic Engineering*, Rotterdam, The Netherlands. <https://doi.org/10.1115/OMAE2011-50329>
- [2] Ji, C. Y., Cheng, Y., Yan, Q., Wang, G., 2016. Fully coupled dynamic analysis of a FPSO and its MWA system with mooring lines and risers. *Applied Ocean Research*, 58, 71-82. <https://doi.org/10.1016/j.apor.2016.03.008>
- [3] Goncalves, E., Nunes, D.C.A., Fernandes, A.O., Testa, G.R., 2000. Vertical load anchor project. *The Tenth International Offshore and Polar Engineering Conference*, Seattle, Washington.
- [4] Liu, H. B., Zhao, C. Y., Ma, G., He, L. X., Sun, L. P., Li, H., 2022. Reliability assessment of a floating offshore wind turbine mooring system based on the TLBO algorithm. *Applied Ocean Research*, 124, 103211. <https://doi.org/10.1016/j.apor.2022.103211>
- [5] Gaidai, O., Xu, X. S., Sahoo, P., Ye, R. C., Cheng, Y., 2021. Extreme hawser tension assessment for FPSO vessel during offloading operation in Bohai bay. *Marine Structures*, 76, 102917. <https://doi.org/10.1016/j.marstruc.2020.102917>
- [6] Alkan, S., 2022. Enhancement of marine corrosion and tribocorrosion resistance of offshore mooring chain steel by aluminizing process. *Brodogradnja*, 73(4), 131-159. <https://doi.org/10.21278/brod73407>
- [7] Mentés, A., Yetkin, M., 2022. An application of soft computing techniques to predict dynamic behaviour of mooring systems. *Brodogradnja*, 73(2), 121-137. <https://doi.org/10.21278/brod73207>
- [8] Ehlers, C. J., Young, A. G., 2004. Technology assessment of deepwater anchors. *Offshore Technology Conference*, Houston, Texas. <https://doi.org/10.4043/16840-MS>
- [9] Degenkamp, G., Dutta, A., 1989. Soil resistances to embedded anchor chain in soft clay. *Journal of Geotechnical Engineering*, 115(10), 1420-1438. [https://doi.org/10.1061/\(ASCE\)0733-9410\(1989\)115:10\(1420\)](https://doi.org/10.1061/(ASCE)0733-9410(1989)115:10(1420))
- [10] Neubecker, S. R., Randolph, M.F., 1994. Model testing and theoretical analysis of drag anchors in sand. *94th International Conference Centrifuge*, Singapore.
- [11] Dahlberg, R., Strom, P. J., 1999. Unique onshore tests of deepwater drag-in plate anchors. *Offshore Technology Conference*, Houston, Texas. <https://doi.org/10.4043/10989-MS>
- [12] Heyerdahl, H., Eklund, T., 2001. Testing of plate anchors. *Offshore Technology Conference*, Houston, Texas. <https://doi.org/10.4043/13273-MS>
- [13] Liu, H. X., Zhang, W., Zhang, X. W. and Liu, C. L., 2010. Experimental investigation on the penetration mechanism and kinematic behaviour of drag anchors. *Applied Ocean Research*, 32(4), 434-442. <https://doi.org/10.1016/j.apor.2010.09.004>
- [14] Fanning, J., 2020. Plate anchors for offshore foundations in sand and clay. *Queen's University Belfast Press*, Northern Ireland, United Kingdom.

- [15] Liu, H. X., Huang, W., Lian, Y. S., Li, L. N., 2014. An experimental investigation on nonlinear behaviors of synthetic fiber ropes for deepwater moorings under cyclic loading. *Applied Ocean Research*, 45, 22-32. <https://doi.org/10.1016/j.apor.2013.12.003>
- [16] Lian, Y. S., Liu, H. X., Huang, W., Li, L. N., 2015. A creep–rupture model of synthetic fiber ropes for deepwater moorings based on thermodynamics. *Applied Ocean Research*, 52, 234-244. <https://doi.org/10.1016/j.apor.2015.06.009>
- [17] Gaudin, C., Simkin, M., White, D. J., O'Loughlin, C. D., 2010. Experimental investigation into the influence of a keying flap on the keying behaviour of plate anchors. *Proceedings of the 20th International Society of Offshore and Polar Engineering Conference*, Beijing, China.
- [18] Neubecker, S. R., Randolph, M. F., 1996. The performance of drag anchor and chain systems in cohesive soil, *Marine Georesources and Geotechnology*. 14, 77–96. <https://doi.org/10.1080/10641199609388305>
- [19] Ruinen, R. M., 2004. Penetration analysis of drag embedment anchors in soft clays. *Proceedings of the 14th International Offshore and Polar Engineering Conference*, Toulon, France.
- [20] Aubeny, C. P., Murff, J. D., 2008. Prediction of anchor trajectory during drag embedment in soft clay. *International Journal of Offshore and Polar Engineering*, 18(4), 314-319.
- [21] Peng, J. S., Liu, H. X., Liang, K., Xiao, Z., 2021. A theoretical model for analyzing the behaviour of drag anchors in layered soils. *Ocean Engineering*, 222, 108568. <https://doi.org/10.1016/j.oceaneng.2021.108568>
- [22] Ma, G., Sun, L. P., Wang, H. W., 2014. Implementation of a visco-elastic model into slender rod theory for deepwater polyester mooring line. *Proceedings of the ASME 2014 33rd International Conference on Ocean, Offshore and Arctic Engineering*, San Francisco, California, USA. <https://doi.org/10.1115/OMAE2014-23594>
- [23] Wang, L. Z., Shen, K. M., Li, L. L., Guo, Z., 2014. Integrated analysis of drag embedment anchor installation. *Ocean Engineering*, 88, 149-163. <https://doi.org/10.1016/j.oceaneng.2014.06.028>
- [24] Cong, B. L., Wang, Z. T., Chan, A. H. C., Yang, Q., 2017. Analytical model for vertically loaded anchor performance with a bridle shank. *Computers and Geotechnics*, 82, 85-98. <https://doi.org/10.1016/j.compgeo.2016.09.012>
- [25] Wu, X. N., Wang, T., Liao, Q. and Li, Y., 2020. Influence of kinematic analysis parameters of drag anchor trajectory prediction using yield envelope method. *China Ocean Engineering*, 34(2), 257-266. <https://doi.org/10.1007/s13344-020-0024-6>
- [26] Hu, Y., Randolph, M. F., 1998. A practical numerical approach for large deformation problems in soil. *International Journal for Numerical and Analytical Methods in Geomechanics*, 22(5), 327-350. [https://doi.org/10.1002/\(SICI\)1096-9853\(199805\)22:5<327::AID-NAG920>3.0.CO;2-X](https://doi.org/10.1002/(SICI)1096-9853(199805)22:5<327::AID-NAG920>3.0.CO;2-X)
- [27] Hossain, M. S., Randolph, M. F., Hu, Y., White, D. J., 2006. Cavity stability and bearing capacity of spudcan foundations on clay. *Proceedings of the Offshore Technology Conference*, Houston, Texas. <https://doi.org/10.4043/17770-MS>
- [28] Zhang, Y. H., Wang, D., Cassidy, M. J., Bienen, B., 2014. Effect of installation on the bearing capacity of a spudcan under combined loading in soft clay. *Journal of Geotechnical and Geoenvironmental Engineering*, 140(7): 04014029. [https://doi.org/10.1061/\(ASCE\)GT.1943-5606.0001126](https://doi.org/10.1061/(ASCE)GT.1943-5606.0001126)
- [29] Qiu, G., Henke, S., Grabe, J., 2011. Application of a Coupled Eulerian-Lagrangian approach on geomechanical problems involving large deformations. *Geotechnique*, 66(11): 1-6. <https://doi.org/10.1016/j.compgeo.2010.09.002>
- [30] Tho, K. K., Leung, C. F., Chow, Y. K., Swaddiwudhipong, S., 2012. Eulerian finite-element technique for analysis of jack-up spudcan penetration. *International Journal of Geomechanics*, 12(1): 64-73. [https://doi.org/10.1061/\(ASCE\)GM.1943-5622.0000111](https://doi.org/10.1061/(ASCE)GM.1943-5622.0000111)
- [31] Yi, J. T., Pan, Y. T., Qiu, Z. Z., Liu, F., Zhang, X. Y., Zhang, L., 2020. The post-installation consolidation settlement of jack-up spudcan foundations in clayey seabed soils. *Computers and Geotechnics*, 123: 103611. <https://doi.org/10.1016/j.compgeo.2020.103611>
- [32] Zhao, Y. B., Liu, H. X., 2016. Numerical implementation of the installation/mooring line and application to analyzing comprehensive anchor behaviours. *Applied Ocean Research*, 54, 101–114. <https://doi.org/10.1016/j.apor.2015.10.007>
- [33] Dou, Y. Z., Yu, L., 2018. Numerical investigations of the effects of different design angles on the motion behaviour of drag anchors. *Applied Ocean Research*, 76, 199-210. <https://doi.org/10.1016/j.apor.2018.05.003>

- [34] Lai, Y., Zhu, B., Huang, Y. H., Chen, C., 2020. Behaviours of drag embedment anchor in layered clay profiles. *Applied Ocean Research*, 101, 102287. <https://doi.org/10.1016/j.apor.2020.102287>
- [35] Zhou, X. K., Chen, J.H., Ge, Z.G., Zhou, T., Li, W. H., 2022. Numerical investigations on the effects of seabed shallow soils on a typical deepwater subsea wellhead system. *Brodogradnja*, 73(3), 1-19. <https://doi.org/10.21278/brod73301>
- [36] McCarthy, K., Young, A., Remmes, B., 1981. Avoiding jack-up rig foundation failures. *Proceedings of Symposium on Geotechnical Aspects of Coastal and Offshore Structures*, Bangkok.
- [37] Liu, H. X., Peng J. S., Liang, K., Xiao, Z., 2019. The behaviour of anchor lines embedded in layered soils. *Ocean Engineering*, 190, 106424. <https://doi.org/10.1016/j.oceaneng.2019.106424>
- [38] Peng, J.S., Liu, H.X., 2019. Analytical study on comprehensive behaviors of drag anchors in the seabed. *Applied Ocean Research*, 90, 101855. <https://doi.org/10.1016/j.apor.2019.101855>
- [39] Lai, Y., Zhu, B., Huang, Y.H., Chen, C., 2020. Behaviours of drag embedment anchor in layered clay profiles. *Applied Ocean Research*, 101, 102287. <https://doi.org/10.1016/j.apor.2020.102287>
- [40] *Dassault Systemes* (2014), ABAQUS, version 6.14.
- [41] Qiao, D. S., Guan, B., Liang, H. Z., Ning, D. Z., Li, B. B., Ou, J. P., 2020. An improved method of predicting drag anchor trajectory based on the finite element analyses of holding capacity. *China Ocean Engineering*, 34(1), 1-9. <https://doi.org/10.1007/s13344-020-0001-0>
- [42] Li, Y., Liu, L.Q., Guo, Y., Deng, W. R., 2022. Numerical prediction on the dynamic response of a helical floating vertical axis wind turbine based on an aero-hydro-mooring-control coupled model. *Energies*, 15(10), 3726. <https://doi.org/10.3390/en15103726>
- [43] White, D. J., Gaudin, C., Boylan, N., Zhou, H., 2010. Interpretation of T-bar penetrometer tests at shallow embedment and in very soft soils. *Canadian Geotechnical Journal*, 47(2), 218-229. <https://doi.org/10.1139/T09-096>

Submitted: 10.02.2023. Bin Wang, binwangdut@outlook.com
Key Laboratory of Far-shore Wind Power Technology of Zhejiang Province,
Hangzhou 311122, China.

Accepted: 06.04.2023. Yuqi Jiao, jiaoyq@mail.dlut.edu.cn
State Key Laboratory of Coastal and Offshore Engineering, Dalian University
of Technology, Dalian 116024, China
Dongsheng Qiao, (Corresponding author) qiaods@dlut.edu.cn
State Key Laboratory of Coastal and Offshore Engineering, Dalian University
of Technology, Dalian 116024, China
Shan Gao, gao_s3@hdec.com
Key Laboratory of Far-shore Wind Power Technology of Zhejiang Province,
Hangzhou 311122, China.
Powerchina Huadong Engineering Corporation Limited, Hangzhou 311122,
China
Tianfei Li, li_tf@hdec.com
Powerchina Huadong Engineering Corporation Limited, Hangzhou 311122,
China
Jinping Ou, oujinpings@dlut.edu.cn
State Key Laboratory of Coastal and Offshore Engineering, Dalian University
of Technology, Dalian 116024, China